Simulation of multimodal optical coherence tomography for biomedical diagnostics: comprehensive full-wave description based on ballistic scattering of arbitrary-profile beams

Alexander L. Matveyev, Lev A. Matveev, Aleksandr A. Moiseev, Alexander A. Sovetsky, Grigory V. Gelikonov, Vladimir Y. Zaitsev

Institute of Applied Physics, Russian Academy of Sciences, 603950 Ulyanova Str., 46, Nizhny Novgorod, Russia

matveyev@ipfran.ru; lev@ipfran.ru; aleksandr.moiseev@gmail.com; alex.sovetsky@ipfran.ru; grig@ufp.appl.sci-nnov.ru; vyuzai@ipfran.ru

Abstract: We present a computationally efficient full-wave spectral model of OCT-scan formation with the following capabilities/features: (i) the illuminating beam may have arbitrary phase-amplitude profile with allowance of a sharp diaphragm; (ii) paraxial approximation that limits the degree of focusing/divergence is not used; (iii) the broadly used approximation of ballistic (single) scattering by discrete scatterers is assumed without additional limitations on the density of scatterers, their distribution in space and scattering strengths with possible frequency-dependence; (iv) besides rigorous accounting for the influence of focusing/divergence of the waves, factors describing the wave decay can readily be introduced by analogy with Monte-Carlo approaches; (v) arbitrary measurement noises can easily be added to simulate required signal-to-noise ratios. The model also allows one to account for arbitrary (e.g., random or flow/deformation-induced) displacements of scatterers between subsequently generated scans. Thus, in view of the above-listed features the model can be characterized as comprehensive in the framework of ballistic scattering by discrete scatterers. The model is computationally efficient due to the use of only rapid summations and fast Fourier transforms. Main model features are illustrated, including simulations of OCT scans for a nearly non-diverging Bessel beam and a focused Gaussian beam, with the possibility to introduce at the tissue boundary arbitrary aberrations represented via Zernike polynomials often utilized for describing aberrations in ophthalmology. The unprecedented flexibility and high computational efficacy of the model open a broad range of possibilities for studying OCT-scan properties and developing new methods of their processing for biomedical diagnostics.

Keywords: Optical coherence tomography; OCT; OCT-image formation; Numerical simulation of OCT; Multimodal OCT

1. Introduction

OCT signal simulation suggests unique possibilities for development/optimization of various OCT modalities in highly controllable, easily modifiable conditions, which cannot be attained in physical experiments with real biological tissues and even phantoms. Numerous research groups make significant effort in developing various tools to enable modeling of OCT signals for general and specific purposes, e.g.[1-12]. Main approaches to OCT-scan modeling roughly can be divided in such groups as Monte-Carlo methods[2,4,5], utilization of the point-spread function concept[11,12] and full-wave methods describing in various approximations the forward propagation of the optical wave towards scatterers and then its backward propagation and collection over the receiving aperture[6,7,8].

In many models the scatterers are approximated by discrete scattering centers, properties of which can be more complex than point scatterers (e.g., accounting for frequency dependence) to better imitate real tissues. The use of discrete scatterers concerns all three groups of simulation methods (e.g.[9,16,17,18]). This is quite a meaningful approximation, even if real scatterers are not literally point-like objects; nevertheless, they still can be treated as discrete sub-resolution particles in OCT scans and be reasonably corresponded to cells in biological tissues. Also it should be recalled that the very fact of successful realization of OCT imaging is based on utilization of ballistic back-scattering. Even within the single-scattering approximation one can study many important specific features of OCT images (e.g., evolution of speckle patterns in the presence of scatterer motions, statistical properties of OCT speckles, etc.). Multiple

scattering as a degrading factor in OCT often is of secondary interest, because numerous OCT-scan features can be well captured even in the single-scattering approximation. It is noteworthy that, depending on the situation, speckles in OCT may be either considered as a degrading factor or play a useful role of high diagnostic value[1]. For instance, motion-induced speckle variability is the basis of OCT-angiography[19]. Therefore, it is reasonable that the majority of scan-formation models in OCT are based on ballistic approximation.

For the illuminating-beam description in such models, usually various additional simplifications are made, which may be more or less realistic. In simpler variants like[1,16], the illuminating beams may have uniform phase in the cross section (which still may be a reasonable simplification for OCT-systems with weakly focused beams without pronounced curvature of wave fronts, whereas the amplitude profile may be variable, e.g. Gaussian). Even using such simplified beam geometries as in[13,16], it is already possible to simulate important features of real OCT-scans formed by beams with weak focusing/divergence and obtain useful results for developing new OCT modalities such as elastography[20,21,22,23]. For weakly focused beams, the validity of such simplified models is also confirmed by similarity with physical experiments and results of more advanced models like[17,18] that belong to full-wave approaches and are based on rigorous consideration of Gaussian beams with allowance for pronounced focusing.

It should be pointed out that for simulations of realistic densities of scatterers (imitating the density of cells in biological tissues) in biologically relevant sizes of visualized regions (~hundreds of microns and greater), sufficiently high computational efficacy of the simulations is of key importance, especially when large series of OCT-data volumes are required to study effects of moving scatterers. In this context utilization of Gaussian beams in modeling is rather attractive because of the possibility to describe their forward propagation analytically. Collection of the back-propagated waves over the receiving aperture can be made either using numerical integration (like in[17]), or even analytically for non-diaphragmed beams[18]. Certainly, the possibility to pass from numerical integration to analytical description of the back-propagated wave and its collection over the receiving aperture like in[18] dramatically improved the computational efficiency. However, this improvement was enabled at the expense of a limitation: the Gaussian beam diameter should be significantly smaller than the illuminating/receiving aperture. For non-Gaussian beam forms (and even for a Gaussian beam with an aperture limited by a diaphragm or somewhat distorted by aberrations), feasibility of analytical description of the illuminating-beam propagation towards scatterers becomes either impossible or requires a radical reformulation of all basic equations. Numerical realizations (concerning both the forward/backward propagation and collection of the backscattered fields over the receiving aperture) is very computationally demanding. Consequently, development of realistic and flexible models of OCT-scan formation requiring minimal simplifications/approximations and at the same time enabling high computationally efficiency remains challenging and highly demanded.

In what follows we demonstrate that using the same basic approximations (i.e., the use of discrete scatterers and ballistic scattering) as in[17,18] and many other models, e.g.[9,14], it is possible to reformulate the OCT-scan formation model, such that the above-mentioned limitations can be completely lifted. As a result, the modified model acquires the following previously unavailable features: (i) it may simulate OCT scans using *arbitrary illuminating beams* (Gaussian, Bessel, etc.), including the possibility to introduce sharp diaphragms; (ii) *arbitrary aberrations* of the illuminating beam can be introduced (such that forward and backward propagation through the aberrating screen is rigorously accounted for); (iii) the widely accepted *paraxial approximation is not required*, so that wide-angle beams can be used; (iv) arbitrary motions of scatterers between subsequent scans can be readily accounted in the model; (v) although the widely used approximation of ballistic scattering at discrete scatterers is used, there are no other limitations on the density of scatterers, their distribution in space and scattering strengths including possible frequency-dependence.

The proposed modified model described in the next section uses full-spectral representation of the illuminating/scatterered fields (both in axial directions, like is physically used in spectral-domain OCT, and the description of the transversal profile of the wave is also made in the spectral form instead of the spatial-domain representation). Due to such a modification, the new formulation of the model becomes very straightforward and strikingly compact. The possibility of using arbitrary beam profiles is not made at the expense of computational

efficiency; on the contrary, the model computationally is very fast. To the best of our knowledge, there were no previously discussed models that could simultaneously suggest such a range possibilities.

Then we demonstrate the possibilities of the proposed model, initially by validating it via comparison with the reference model[18] that is based on *exact analytical solutions* for non-diaphragmed focused Gaussian beams. We demonstrate that in approximation of sufficiently large aperture (required for validity of[18]) for the same set of scatterers, the proposed new formulation yields the results coinciding with a high accuracy with the exact analytical results[18]. The universality of the new model is then illustrated by obtaining OCT images for a Gaussian beam and a Bessel one (again for the same set of scatterers). Furthermore, in view of high importance of accounting for aberrations for some applications of OCT (e.g., in ophthalmology[24]), the unique flexibility of the new model is demonstrated by generating images with additionally introduced aberrations represented by Zernike functions often used for descriptions of eye-lens aberrations in ophthalmology. Finally, the model usage in configuration with moving scatterers (like in angiographic/elastographic applications) is demonstrated.

2. Methods of full-wave spectral description of OCT-scan formation

In the proposed description, each spectral component of the illuminating-beam with wavenumber k is characterized by a complex-amplitude distribution $L(x,y,k)$ at the output lens (with allowance for a sharp diaphragm). The lens is located in the (x,y) plane has the axial coordinate $z=z_d$ and z-axis is directed to the tissue depth along the axis of the illuminating beam as shown in Fig. 1. Coordinate z_d may either directly correspond to the tissue boundary or the boundary of the immersion layer (in which scatterers are absent). The lateral coordinates (x_0,y_0) of the beam axis define the position of a single A-scan, so that lateral scanning required for obtaining 3D volume of OCT data corresponds to variation in (x_0,y_0). Each discrete scatterer is characterized by coordinates (x_s,y_s,z_s). Like in real spectral-domain OCT we represent the illuminating beam as a set of spectral components with wavenumbers k. The forward propagation of the axial spectral components and their back-propagation from scatterers is often described in the spatial domain[17,18]. However, in principle the spectral approach can be used to describe the optical-wave evolution in axial direction as well. For example, after obtaining 3D images in[17,18], the numerical refocusing was made by recalculating the wave fronts considering their spatial spectra in the lateral direction. In what follows we apply such a spectral-domain description (both in the axial and lateral directions) to describe the wave fields for all stages: first, for illuminating-beam propagation towards the scatterers and then for backward propagation of scattered fields and their collection over the illuminating-receiving aperture.

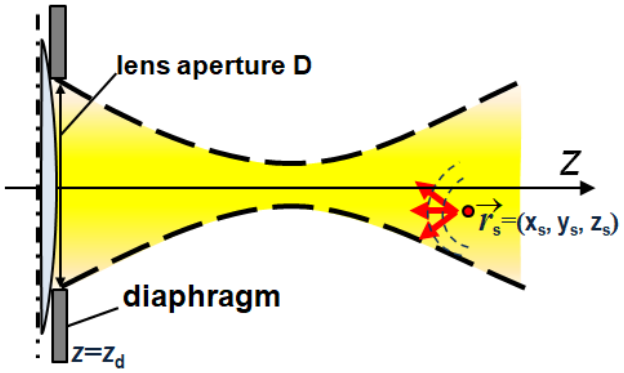

Fig. 1. Schematically shown geometry of the illuminating beam (not necessarily focused like in the figure) with the lateral coordinates (x_0,y_0) of the axis directed to the tissue depth along the z-axis of the coordinate system. Coordinates (x_s,y_s,z_s) characterize positions of scatterers.

In such a representation, the complex-amplitude distribution $L(x,y,k)$ over the input/output aperture is characterized by the spatial spectrum $g(u,v,k)$ (for simplicity, below we omit constant factors before the integrals):

$$g(u,v,k) = \iint\limits_{x,y\in D} L(x,y,k)e^{-i(ux+vy)}dxdy\,. \tag{1}$$

Here, for brevity we denote the wave vector projections $k_x = u$ and $k_y = v$.

After propagation of the illuminating beam between the input plane $z = z_d$ and plane $z = z_s$ corresponding to the depth of a scatterer with coordinate z_s, the illuminating-wave spectrum can be written as $h_s(u,v,k)g(u,v,k)$, where the propagator function $h_s(u,v,k)$ has the form

$$h_s(u,v,k) = e^{i(z_s-z_d)\sqrt{k^2-u^2-v^2}}\,. \tag{2}$$

Note that a similar method for describing the axial evolution of the transversal spectrum of the illuminating beam using the propagator (2) was recently applied in paper[15] to describe degradation of the point-spread function in the presence of refractive-index fluctuations. Since for the scatterer with coordinates (x_s, y_s, z_s), the transversal spatial spectrum of the incident wave is $h_s(u,v,k)g(u,v,k)$, its Fourier transform over spectral coordinates (u,v) corresponds to the spatial-domain representation of the field incident on the scatterer:

$$U_s(x_0,y_0,k) = \iint\limits_{u^2+v^2\le k^2} g(u,v,k)h_s(u,v,k)e^{i[u(x_s-x_0)+v(y_s-y_0)]}dudv\,, \tag{3}$$

The possibility to describe the field $U_s(x_0,y_0,k)$ in the spectral form (3) is a very useful feature, because the transversal spectrum $g(u,v,k)$ can be readily found numerically for an *arbitrary* beam profile $L(x,y,k)$ only once for all scatterers and does not require additional assumptions (e.g., about a Gaussian profile, absence of a diaphragm, etc.) which are usually needed to simplify analytical consideration.

In can also be noted that by analogy with the spectral function $g(u,v,k)$ defined by Eq.(1) (i.e., the Fourier transform of the initial beam profile $L(x,y,k)$), for the propagator $h(u,v,k)$ in the spectral form, its spatial-domain counterpart $H_s(x,y,k)$ can be introduced via the inverse Fourier transform over spectral coordinates (u,v):

$$H_s(x,y,k) = \iint h_s(u,v,k)e^{i(ux+vy)}dudv \tag{4}$$

Bearing in mind that according to Eq.(3), the transversal spectrum of $U_s(x_0,y_0,k)$ is given by the product of the Fourier transforms $g(u,v,k)$ and $h_s(u,v,k)$ corresponding to the spatial-domain functions $L(x,y,k)$ and $H_s(x,y,k)$, according to the theorem about the product of spectra, function $U_s(x_0,y_0,k)$ can also be expressed as the following convolution of $L(x,y,k)$ and $H_s(x,y,k)$:

$$U_s(x_0,y_0,k) = \iint\limits_{x,y\in D} L(x-x_0,y-y_0,k)H_s(x_s-x,y_s-y,k)dxdy \tag{5}$$

In Eq.(5) the integral is found over the aperture D of the lens (see Fig. 1). In fact $H_s(x,y)$ is the Green's function for a localized scatterer located at (x_s, y_s, z_s) and Eq. (5) is a spatial-domain counterpart of the spectral representation of the incident wave given by Eq. (3).

The scattered wave for a discrete scatterer located at (x_s, y_s, z_s) is proportional to the incident-wave amplitude $U_s(x_0, y_0, k)$. This scattered field propagates back to the illuminating/receiving aperture and is collected by the lens, which is again described the convolution of the Green's function and receiving aperture similarly to Eq.(5). Then the amplitude $B_s(x_0, y_0, k)$ of the spectral component with wave number k collected at the receiving aperture is

$$B_s(x_0, y_0, k) = U_s(x_0, y_0, k) \iint\limits_{x,y \in D} L(x - x_0, y - y_0, k) H_s(x_s - x, y_s - y, k) dxdy \tag{6}$$

Here, the pre-integral factor corresponds to the incident-field amplitude, whereas the integral factor describing the collection of the back-scattered wave is identical to integral in Eq.(5) that describes the forward propagation. In view of this, Eq.(6) cab be rewritten in the compact form as the incident field squared:

$$B_s(x_0, y_0, k) = U_s^2(x_0, y_0, k). \tag{7}$$

At this point it should be recalled that Eq.(6) describes the received amplitude $B_s(x_0, y_0, k)$ for a single spectral component with the wavenumber $k = k_n$, whereas in spectral-domain OCT, the optical-beam contains a large number of illumination spectral components $\exp(ik_n z)$ with wavenumbers k_n. In previous papers[16,17,18] (where spectral amplitudes $B_s(x_0, y_0, k)$ were found differently than described above) we discussed in detail that superposition of $n = 1..N$ spectral components with wavenumbers k_n forms a pixelated A-scan composed of $q = 1..N$ pixels. This superposition mathematically corresponds to Fourier transformation over the axial wavenumbers, which is performed in spectral-domain OCT scanners to form in-depth A-scans. Using the notations similar to those used in works[16,17,18] we can write the following expression for the complex-valued amplitude $A(x_0, y_0, z_q)$ of q-th pixel with the axial (depth) coordinate z_q and coordinates (x_0, y_0) in the lateral plane:

$$A(x_0, y_0, z_q) = \sum_n \sum_s B_s(x_0, y_0, k_n) S(k_n) \exp\left(-i \frac{2\pi n}{H} z_q\right) \tag{8}$$

In Eq.(8) summation is made for the contributions of all spectral harmonics $n = 1..N$ also taking into account their amplitudes $S(k_n)$ in the illuminating-beam spectrum. The second summation in Eq.(8) is made over contributions of all scatterers located within the beam. In a more compact form Eq.(8) can be written as the Fourier transform over k_n

$$A(x_0, y_0, z_q) = FFT_{k_n}\left\{\sum_s S(k_n) B_s(x_0, y_0, k_n)\right\}, \tag{9}$$

where the spectral form $S(k_n)$ of the illuminating beam is explicitly retained.

It should be emphasized that although spectral Eq.(3) and spatial-domain Eq. (5) equivalently represent the same amplitude $U_s(x_0, y_0, k)$, the possibility of its efficient evaluation in the spectral form (3) *is the central point for computational efficiency* of the described model. Indeed, spectrum $g(u, v, k)$ readily allows one to represent an *arbitrary phase-amplitude form* $L(x, y, k)$ of the illuminating beam via Eq.(1). Therefore, the spectral representation confers the

above-described model unprecedented computational speed for treating arbitrary initial beam profiles $L(x,y,k)$ without radical reformulation. In particular, not only Gaussian beams, but other beam forms can be used (e.g., Bessel or Laguerre-Gauss beams that attract high interest in recent years). Also aberrations of the illumination beam at the boundary of the visualized region can easily be introduced, which is of interest for OCT applications in ophthalmology, etc. For any beam profile $L(x,y,k)$, the transversal spectrum $g(u,v,k)$ should be found only once and used for all A-scans and scatteres. Next, it should be pointed out that the spectral representation of the propagator $h_s(u,v,k)$ can be used in the exact form (2) and *does not require the use paraxial approximation*, which is often necessary for obtaining analytical results in other models.

Finally, *one can readily imitate motions of scatterers* by varying coordinates of scatterers (x_s, y_s, z_s) for subsequently obtained scans. Notice that for motionless scatterers, estimation of Fourier transform given by Eq. (3) can be made using rapid FFT-algorithms to obtain (via Eqs. (7) and (8)) spectral amplitudes $B_s(x_0, y_0, k)$ for the entire set of A-scan positions (x_0, y_0) within the simulated 3D volume of OCT-data. For displaced scatterers, the data should be recalculated and the total computation time will depend on the total number of (x_0, y_0)-coordinates of the illuminating beam within the 3D data set and the required number of recalculations for moving scatterers. Depending on their velocities, for certain cases, displacements may be sufficient to consider either between entire 3D volumes, in other cases variations in (x_s, y_s, z_s) may be significant even on inter-A-scan intervals requiring larger amount of recalculations. In the next section we present examples of utilization of the proposed model to illustrate its main new features/capabilities.

3. Simulation examples to demonstrate main model capabilities

In the below-presented examples we assume that the central wavelength of the OCT system is 1.3 μm and spectral width is 90 nm, which are "typical" parameters for OCT. Similarly to[18] we simulate the OCT data for rectangular volumes with sizes 128x128x128 pixels corresponding to biologically-relevant physical sizes of 512 μm in depth and 192 μm in the lateral directions. Other parameters of the illuminating beam and scatterers are specified for each of the examples.

First, for validation of the proposed model, it makes sense to compare the result of the new spectral formulation given by Eqs. (1), (3), (7) and (9) with the reference model[18], because the latter is based on *exact* analytical solutions for the spectral amplitudes $B_s(x_0, y_0, k)$ obtained for a non-diaphragmed Gaussian beam (i.e., assuming that the lens aperture is sufficiently big and can be considered infinite). For comparison of the present model with[18], we accepted identical parameters of a focused Gaussian beam and generated scans for a set of 7 scatterers with identical lateral coordinates and different depths, including the focal depth $z = 128$ μm. Figures 2a and 2b demonstrate that the described full spectral-domain formulation based on discrete Fourier transforms gives the spatial forms of point-spread functions very close to the results obtained using the exact analytical model[18]. The depth profiles shown in Fig. 2c confirm that the two methods demonstrate excellent coincidence of the signal amplitude, so that minor differences can be observed only in low-amplitude zones (at a level about -60 dB below the maxima and lower) sufficiently far from the scatterers. This coincidence with the exact analytical results for a pronouncedly focused Gaussian beam confirms the reliability of the proposed model, for which, however, the main new feature is the ability to describe OCT signals formed by *arbitrary* beams, not necessarily axially symmetric ones.

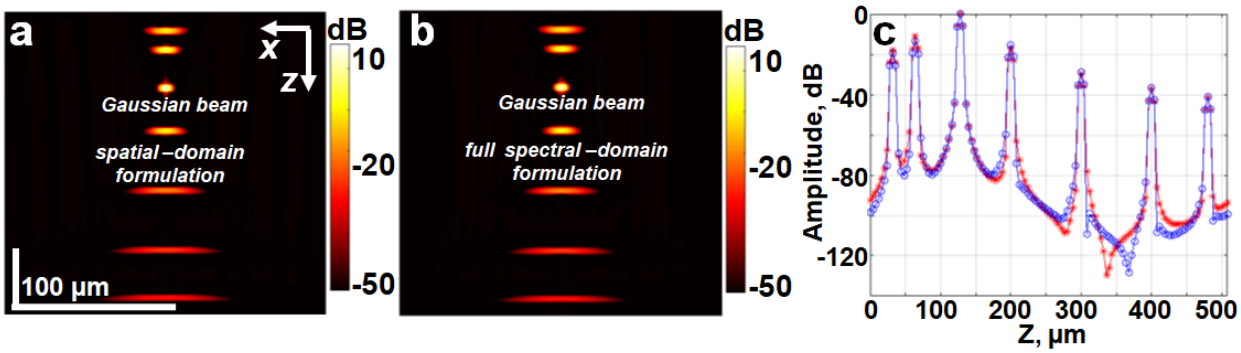

Fig.2. Comparison of OCT images for the same set of scatterers and the same pronouncedly focused Gaussian beam simulated using: (a) reference model[18] (based on exact analytical solutions obtained in spatial domain for Gaussians beams) and (b) the present universal model formulated in spectral domain. (c) shows the depth profiles along the beam axis for the two models (asterisks are for model[18] and circles correspond to the present model).

The following examples demonstrate that the ability of the model to describe arbitrary beams opens the possibility to efficiency simulate various aberrations. Such aberrations may characterize, for example, the eye cornea, which is of interest for ophthalmic applications of OCT. In the following examples, the aberrations are modeled by introducing phase distortions of an initially Gaussian beam. Again, to clearer demonstrate how various aberration alter the PSF form, we intentionally took a small number (ten) scatterers located at a depth of the focal plane, which may be considered as imitation of focusing at the eye retina. Figure 3 demonstrates the simulated scans in (x,y)-plane (C-scans) without (panel (a)) and with aberrations of several characteristic types (Figs 3b, 3c and 3d). Such aberrations may arise in OCT- imaging of the eye retina surface through cornea and eye lens with imperfect refraction [24], phase distortions of which are often approximated by a set of Zernike polynomials [25]). It is clear from Fig. 3 that both worsening of the PSF-localization in the focal plane and aberration-induced translational shifts of the entire C-scan can readily be simulated. Such OCT images with *a priori* known aberrations can be used for development and comparison of aberration-correction procedures, which is important, e.g., for improving the quality of OCT-imaging for ophthalmic applications [24,26,27,28] (a special discussion of utilization of simulated OCT images for such applications will be published later).

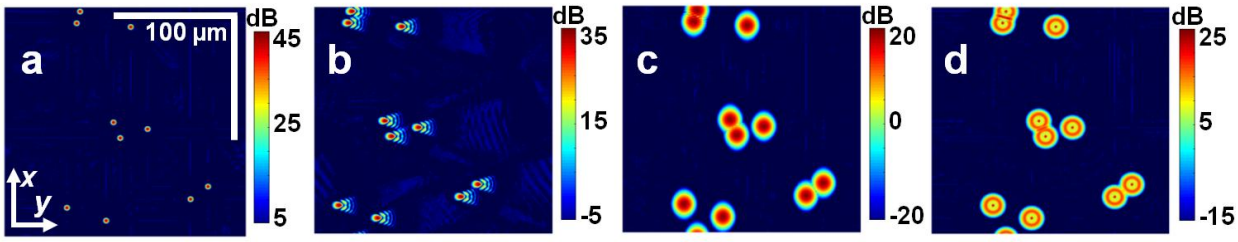

Figure 3. Examples of simulated OCT C-scans in (x, y) plane corresponding to the focus depth $z = 128$ μm for a focused Gaussian beam similar to that, for which (x, z) images in Fig. 2 were shown. Panel (a) with well-localized scatterer images is for the absence of aberrations; (b) is for the aberration corresponding to the Zernike polynomial Z_3^1 (coma); (c) is for the Zernike polynomial Z_2^2 (2nd astigmatism); (d) is for Zernike polynomial Z_6^0 (2nd spherical aberration).

Further, the ability of the model to easily simulate non-Gaussian beams is demonstrated for a Bessel beam (such beam attract significant interest in OCT due to nearly non-diverging character of propagation[29]). We imitated formation of such a beam due to propagation of an initially planar beam with a Gaussian amplitude profile $\exp(-r_\perp^2 / a^2)$ through a

cylindrical axicone with the opening angle 2γ (ref. 30). To this end we introduced in the input plane $z = z_d$ a radially-dependent factor $\exp[ik_n r_\perp tg(\gamma)]$ describing the phase delay acquired by the spectral components of the beam after propagating through the axicone. In the B-scans shown in Fig 4a-1 and 4b-1 we again intentionally used a small number (six) scatterers located at three depths. Figure 4 clearly demonstrates the difference between the propagation of the simulated Bessel beam (row (b) in Fig. 4) and a Gaussian beam with a similar radius of the focal area (row (a) in Fig 4). The Gaussian beam demonstrates pronounced focusing and strong broadening of the PSF outside the focal depth. In contrast, the Bessel beam demonstrates good conservation of the beam-kernel radius, which is accompanied by slow evolution of the surrounding rings corresponding to the Bessel-function sidelobes (compare the C-scans in rows (a) and (b)).

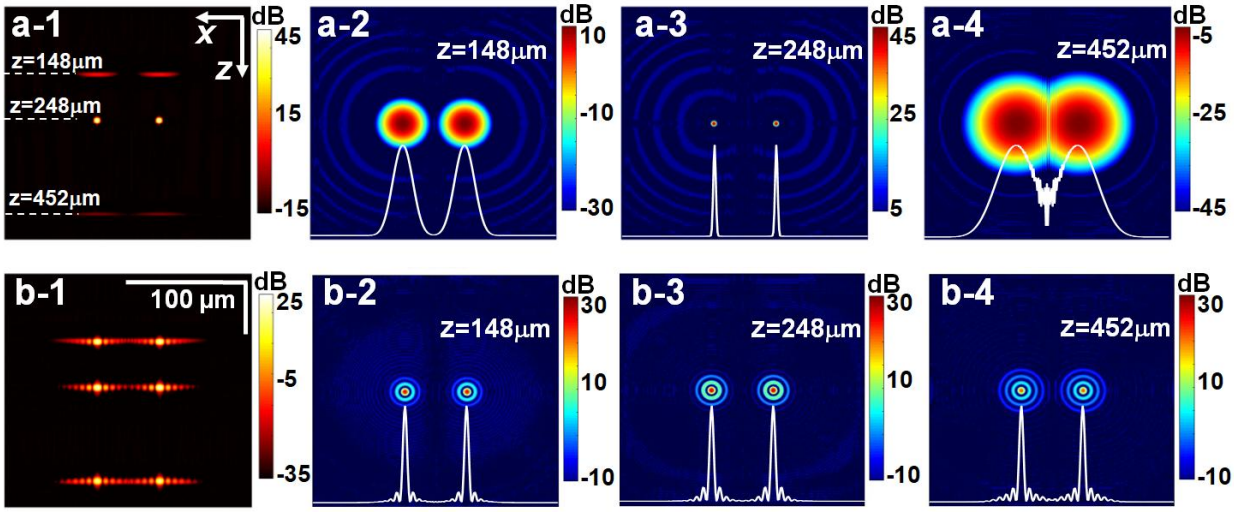

Figure 4. Examples of OCT B-scans in (x, z) plane (first column) and C-scans in (x, y) plane (2nd through 4th columns) at three depths simulated for a Gaussian beam (panels (a-1) through (a-4)) and a Bessel beam (panels (b-1) through (b-4)). It is clear that, for the Gaussian beam, the minimal size of the PSF corresponds to the focal depth $z = 248$ μm, whereas outside the focal depth the PSF sizes are much greater, such that for $z = 452$ μm, the two scatterers are hardly resolved. In contrast, the Bessel beam at all three depth has nearly invariable size of the central kernel, whereas the outer ring-shape sidelobes described by the Bessel function gradually evolve remaining at least 19 dB lower than the amplitude at the axis.

The next examples demonstrate the intrinsic ease of the proposed model to simulate 3D data formed by illuminating beams with arbitrary degree of focusing, which can be used for development/verification of methods of numerical refocusing. In addition we demonstrate the ease of simulation of various noises (to imitate the noise at the receiving array). Figures 5a and 5b show examples of the initial OCT image for a highly-focused Gaussian beam before and after numerical refocusing (with the refocusing algorithm used in[31,17]. The density of scatterers is intentionally chosen fairly low to clearer demonstrate different forms of the point-spread function (PSF) near the focal plane and outside it. It is seen that outside the focal depth the weakly localized scatterer images are essentially masked by the measurement noise. However, after performing numerical refocusing one obtains nearly identical highly localized PSF-forms independently of the depth, i.e., maximal possible resolution the same as at the focal depth is enables everywhere. Consequently, the scatterers become well visible against the noise even outside the physical-focus depth ($z = 480$ μm).

Besides simulations of 3D volumes of OCT data for motionless scatterers, the model allows one to readily re-simulate OCT images for arbitrarily displaced positions of scatterers. Such possibilities are important for testing algorithms of OCT-based elastography and angiography in highly controllable conditions with flexibly modifiable parameters. In physical experiments, even using phantoms, it is very challenging to realize such imaging in highly controllable conditions. In this context, the next examples demonstrate simulations of digital refocusing of 3D OCT-data in the

presence of a scatterer flow to imitate the blood flow in a micro-vessel surrounded by the "solid" tissue. The point is that even a fairly slow motion of scatterers may break conditions of constructive interference of scatterer images during refocusing for various positions of broad scanning beams with multiple overlapping. Consequently, after refocusing these moving scatterers produce regions of very low intensity highly contrasted with motionless scatterers. This effect may be used for singling out moving scatterers against the background signal from motionless scatterers. As illustrated by Fig. 5c, the moving and motionless scatterers are indistinguishable before refocusing and Fig. 5d demonstrates that after refocusing the simulated vessel becomes well visible due to strongly reduced signal level. Notice that near the depths of the physical focus, where the PSF has the minimal size and scatterer images nearly do not overlap for neighboring A-scans, refocusing only slightly changes the OCT image. Consequently, the images of moving scatterers do not change their intensity near the focal depth. By this reason, the flow after refocusing becomes visible as a dark channel only sufficiently far from the focal plane, where the initial size of PSF is much larger than in the focal area. However, after refocusing the PSF size become comparable with the focal-spot size everywhere, so that even quite narrow channels with flow can be visualized with a high resolution as illustrated in Fig. 5d.

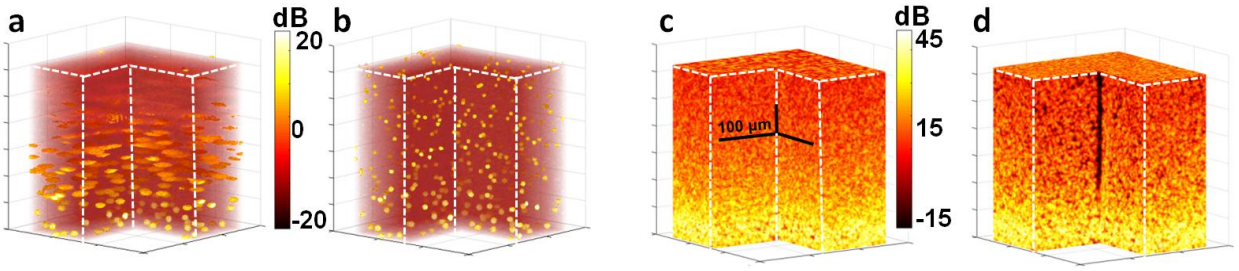

Figure 5. Examples of refocusing of simulated 3D scans for a focused Gaussian beam in the presence of noises and moving scatterers (vertically oriented flow of scatterers). (a) is a 3D image of a rarified set of scatterers to clearer show the difference of highly localized images near the focal plane located closer to the bottom (the focus depth $z = 480$ μm and the focus radius is 3 μm); notice that above the focal depths, the scatterer images are strongly broadened and are nearly masked by the imitated Gaussian "measurement noise" corresponding to SNR~12dB near the focal plane. (b) is the same image after refocusing, due to which the initially defocused scatterer images above the focus depth became well localized and clearly seen against the noise. (c) is a 3D image for a density of scatterers closer to density of biological cells in tissues with an axial flow 10 μm in diameter imitating a blood capillary which is initially indistinguishable against the background; (d) the same refocused image, in which the capillary outside the focal depth becomes well visible with the maximal resolution (corresponding to the focus radius) and looks as a dark channel, which is due to flow-related breaking of the constructive interference in the refocused image; particle displacement between the subsequent A-scans is $\Delta z = 10^{-4}$ μm, which corresponds to the vertical velocity $\Delta z = 4 \cdot 10^{-3}$ m/s for 40 kHz A-scan rate.

Finally, the next example relates to elastographic imaging of local strains in the simulated region, in which a prescribed strain-induced variation in the positions of scatterers is introduced. Strain mapping is the basic step in realization of compression optical coherence elastography (C-OCE)[23] which in recent years opened a broad range of biomedical applications: elastographic differentiation of tumorous versus normal tissue[32,33,34], demonstrations of detailed morphological segmentation of heterogeneous tumor tissues using differences in elasticity among various morphological components[35,36]; studying complex 3D strain fields of thermo-mechanical origin in corneal tissue subjected to laser treatment in the context of refraction correction[37]; detection of insufficient stability of laser-fabricated cartilaginous implants[38]; studying deformations of osmotic origin during tissue impregnation by non-isotonic liquids[39,23]. In view of these very different applications, numerical simulations of exactly controllable arbitrarily complex deformations with possibility to flexibly vary OCT-system parameters, signal-to-noise ratios (SNR), etc., opens unprecedented prospects for detailed multi-parameter studies of elastographic processing in OCT.

For demonstration, in Fig. 6a we show a simulated 3D structural image of a multi-layer structure with various scattering strengths of the layers separated by titled boundaries. Figure 6b shows the prescribed distribution of interframe strains that define axial displacement of scatterers between the initial and deformed states, in which the sample was imaged. The

OCT imaging is simulated for the same highly-focused illuminating beam as used for the examples shown in Fig. 5 with the focus depth $z = 480$ μm. The corresponding rather complex distribution of inter-frame phase variations is shown in Fig. 6c. These interframe variations are found in the absence measurement noises other than the strain-induced "decorrelation noise". However, a very noisy structure of the phase-variations is clearly seen above the focal depth in regions of pronouncedly laterally-inhomogeneous strains. In these regions, large groups of differently displaced scatterers contribute to formation of individual A-scans, so that superposition of waves back-propagated from these scatterers produce very noisy resultant phase variation. The next Fig. 6d shows the phase-variation map obtained after preliminary refocusing, which suppresses this degrading interference of multiple scatterers and yields a much clearer phase-variation map.

In phase-sensitive OCT, the axial-strain distribution can be reconstructed by estimating axial gradients of interframe phase-variations using. These gradients can be found either using conventional least-square fitting[40], or more advanced "vector" method[22,41] that is applied here. The so-reconstructed strain distribution is shown in Fig. 6e that corresponds to directly found noisy interframe phase-variation Fig. 6c. The strain field reconstructed from the phase-variation shown in Fig. 6c demonstrates strong distortions/errors in the regions outside the focus, where the phase variations in the regions of strong lateral inhomogeneity looks very noisy in Fig. 6c. In contrast, the strain map of much better quality shown in Fig. 6f is found using the phase-variation map shown in Fig. 6d after preliminary refocusing. The reconstructed strain map in Fig. 6f is much closer to the exact (assumed) strain distribution (Fig. 6b) with much better quality and uniform lateral resolution over the entire 3D scan.

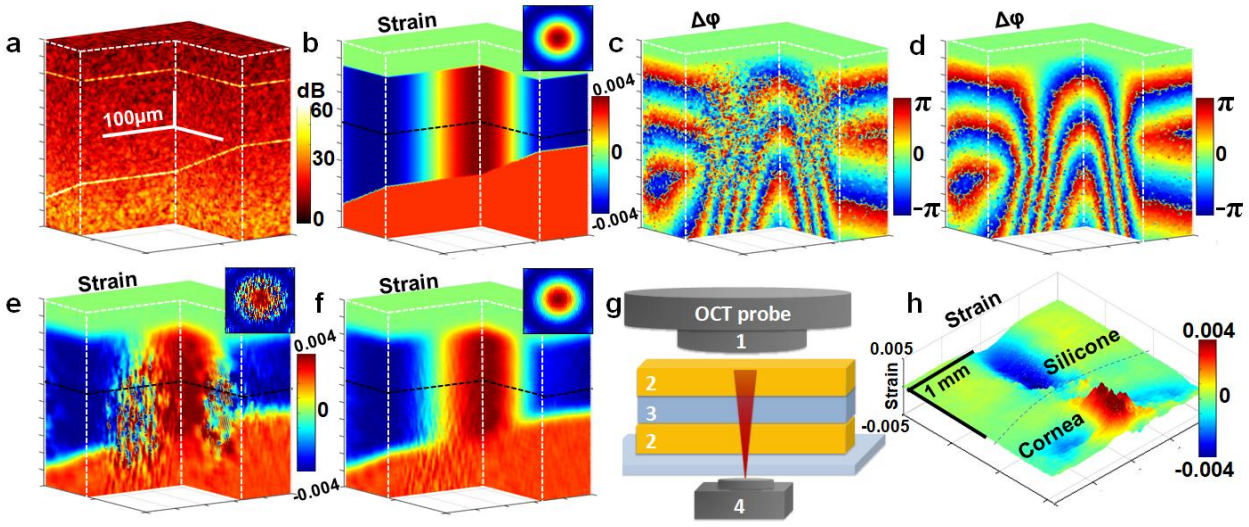

Figure 6. Examples of elastography-related simulations of OCT scans. (a) simulated structural image 192x192x512 microns in size in which the brighter lines separate regions subjected to different straining. (b) the assumed distribution of strains according to which displacements of scatterers were defined (the upper-right inset shows the cross section of the central part of the volume through the plane labeled by the black dashed line. (c) the phase variation between the initial state and final state corresponding to the strain distribution shown in (b). (d) the similar phase-variation map, but obtained with the preliminary performed refocusing of the OCT images in the initial and final states. (e) reconstructed strain distribution based on the noisy phase-variation map (c) found without refocusing. (f) reconstructed strain map based on the phase-variation map (d) found with preliminary performed refocusing. The total amount of scatteres is $2.5 \cdot 10^5$ and the Gaussian beam has the focal depth $z = 480$ μm with the focal-waist radius 3 μm like for Fig. 5. (g) schematically shown a real experimental configuration in which thermomechanical strain distribution similar to the simulated example (b) was experimentally produced (like in works[37,42]): 1- the OCT probe; 2- buffer silicone layers between which the studied samples of cartilaginous or corneal tissues (layer 3) were placed; 4 – infrared laser operating at 1.5 μm that illuminated the samples and produced thermo-mechanical deformations that were partially irreversible and were used for reshaping the tissue. (h) a real example of interframe strains resembling the simulated strain distribution and visualized by processing phase-resolved OCT scans using the vector method[41].

To demonstrate that strain distributions similar to the simulated ones do occur in real situations, Fig. 6g schematically shows such an experimental situation, in which thermo-mechanical strains were produced by irradiating a sample of collagenous tissue (a piece of cartilage or eye cornea) by a beam of infra-red laser. Such studies relate to the development of new methods for non-surgical reshaping of cartilaginous or corneal tissues (see a more detailed discussion in[37,38]). The buffer silicone layers shown in Fig. 6d serve for performing quantitative compression elastography[23] to assess the irradiation-produced variations in the tissue elasticity and make conclusions about the microstructural alterations in the tissue[42]. Figure 6h demonstrates a real experimental example of depth-distribution of interframe laser-induced thermo-mechanical strains with alternate signs in a sandwich sample consisting of rabbit cornea and buffer silicone layers. The strain was reconstructed using the vector method[41]. Such high-resolution OCT-based elastographic imaging based on approach[41] attracts much attention is recent years[43,44], so that the possibility to realistically simulate OCT images of deformed tissues should be very helpful for further perfection of the OCT-based strain/elasticity imaging.

4. Discussion

In the previous section we presented a new form of the OCT-scan formation model and gave several instructive examples demonstrating the main possibilities of the proposed model. Probably, its key new feature is that, despite the very compact formulation, the new model allows for rigorous simulations of arbitrary beam profiles (including sharply diaphragmed beams) and does not require the paraxial approximation. This unique flexibility in utilization of arbitrary phase-amplitude beam profiles suggests very convenient possibilities for modeling arbitrary aberrations (see Fig. 4), which is important in the context of the development/comparison of various methods for their numerical correction. Also various degrees of focusing and qualitatively different types of illumination beams (like Gaussian or Bessel ones in Fig. 3) can efficiently be studied in a uniform manner using Eqs.(1),(3), (7) and (9), in which only the beam profile $L(x, y, k)$ should be changed.

On no less importance are the possibilities of the described new rigorous model to validate the applicability of previously proposed versions of OCT-scan formation models based on various approximations and/or special forms of the beam profile (such as the neglect of the beam-front curvature, assumption of non-diaphragmed Gaussian beams, paraxial approximation, etc.) The point is that such simplified models can enable incomparable computational efficiency in simulations of large sequences of OCT data. Such large sequences are required, e.g., for studying OCT-scan evolution in the presence of flows or Brownian motion of scatterers, or for the development of numerical methods to compensate masking bulk motions of living tissues in OCT-angiography[45,46]. For such applications, more advanced models may either require unacceptable in practice computation time (days and weeks) or utilization of unreasonably expensive (and not necessary in many cases) supercomputing facilities. However, the drawback of approximate/simplified models is that, remaining within the framework of the used approximations, it is impossible to reliably verify the range of parameters, for which these simpler models are applicable. The above-described model readily allows one to validate the applicability of various simplified model formulations such as[16] or model[18] that have already been used for studies of OCT-scan evolution due to variation in the OCT-setup parameters and tissue deformation. For example, they were applied in comparative studies of the correlation-based and phase-resolved elastographic processing of OCT-scans[21] and perfection of strain and displacement reconstruction using phase-sensitive OCT[20,41]. Now the applicability of such models can be reliably validated in fairly arbitrary conditions. Other possibilities, like intrinsic ease in imitating measurement noises (illustrated in Fig. 5) and introducing in the described model the optical-field losses due to absorption and scattering are quite straightforward. By this reason we do not specially focus on these issues.

The main limitation of the described, otherwise rigorous, model is the use of single-scattering (ballistic) approximation. It should be pointed out, however, that the very principle of OCT-visualization is based on this approximation and the multiple-scattering influence in OCT is only one of various degrading factors. Multiple-scattering effect in many cases are of secondary importance, although even degrading of PSF due to multiple forward scattering by refraction-index inhomogeneities can also be introduced in the described approach by analogy with study[15]. In fact for the majority of other model formulations, the neglect of multiple scattering is typical except for Monte-Carlo-based models. The latter

are intrinsically better suitable for considering "snake-like" photon trajectories including multiple scattering, but computationally the Monte-Carlo approach is known to be very demanding. In this context, rather high computational efficiently of the present model can be specially emphasized. Namely, the main Eqs. (1),(3), (7) and (9) rely on Fourier transformations that can be performed using efficient algorithms of discrete fast Fourier transform (FFT). The discrete transversal spectrum $g(u,v,k)$ of an arbitrary beam profile $L(x,y,k)$ should be found only once according to Eq. (1) for a chosen mesh on the (x,y)-plane to represent the positions of A-scans. Then for all of the chosen positions (x_0,y_0), the 2D Fourier transformation over wavenumbers (u,v) in Eq. (3) gives the amplitudes $U_s(x_0,y_0,k_n)$ of the waves incident onto the scatterers. Consequently, all spectral amplitudes $B_s(x_0,y_0,k)$ at the receiving array are immediately found (see Eq.(7)). Then the computationally efficient FFT over the wave-numbers k_n and straightforward summation over all scatterers are performed in Eq. (9), which yields the entire 3D OCT-image.

The required computation time linearly depends to the number of spectral harmonics in the source spectrum $S(k_n)$ (determining the number of pixels in the axial direction). Similarly, the linear proportionality is for the total number of A-scan positions in (x,y)-plane (i.e., the number of pixels in lateral directions) and the total number of scatterers. To give an idea about the required time, simulation of a volume 128x128x128 pixels (corresponding to 192x192 microns laterally and 512 microns in depth) with 250000 scatterers (which is close to the density of biological cells ~5-6 microns in size) requires ~100 min using 10 cores of Intel I-7 6950X CPU. This is about ~twice faster than simulation for the same configuration using the reference model[18] based on the exact analytical expressions found for the special case of non-diaphragmed Gaussian beams. In that model spectral amplitudes $B_s(k_n)$ were analytically found and the simulation of A-scans is reduced to FFT over wave-numbers k_n and summation over contributions of all scatterers like in Eqs.(8) and (9). Nevertheless, for simulation of 3D OCT-scans, the present model has demonstrated comparable and even higher computation efficiency than model[18], but without the requirement to use non-diaphragmed Gaussian beams.

4. Conclusions

In this paper we presented a new form of computationally efficient full-wave model of OCT-scan formation. The model formulation is straightforward and compact with an unique set of capabilities/features: (i) the illuminating beam may have *arbitrary* phase-amplitude profile with allowance of a sharp diaphragm and presence of aberrations; (ii) the model *does not use paraxial approximation* that limits the degree of focusing/divergence of the illuminating beam; (iii) although the broadly used approximation of single (ballistic) scattering by discrete scatterers is assumed, there are no other limitations on the density of scatterers, their distribution in space and scattering strengths with possible frequency-dependence; (iv) besides rigorous accounting for focusing/divergence, factors describing the wave decay can readily be introduced by analogy with Monte-Carlo approaches; (v) arbitrary measurement noises also can easily be added to simulate required signal-to-noise ratios. The model readily also allows one to re-simulate the data for arbitrary changed scatterer position (e.g., random or flow/deformation-induced). Thus, within the framework of ballistic scattering by discrete scatterers, the above-listed intrinsic abilities of the model give reasons to characterize it as comprehensive. The unprecedented flexibility and high computational efficacy of the model open unique possibilities for studying OCT-scan properties and developing novel diagnostic OCT-based modalities for biomedical diagnostics.

Acknowledgements. Basic formulation of the OCT-scan formation model was supported by RFBR grant No 19-02-00645; introducing in the model aberrations and refocusing procedures were developed with support of the RSF grant 17-72-20249.

Conflict of interest: The authors declare no conflict of interest.

Authors' contributions: ALM, GVG and VYZ derived the background equations of the model; AAM and GVG proposed modifications to perform digital refocusing and introduce aberrations; ALM and LAM wrote the code and performed simulations; VYZ, ALM, and AAS prepared the manuscript.

References

1. Schmitt, J.M., Xiang, S.H. & Yung, K.M. Speckle in optical coherence tomography. J. Biomed. Opt. 4(1), 95–105 (1999).
2. Yao, G. & Wang, L.V. Monte Carlo simulation of an optical coherence tomography signal in homogeneous turbid media. Physics in Medicine & Biology. 44(9), 2307 (1999).
3. Duncan, D.D. & Kirkpatrick, S.J. The copula: a tool for simulating speckle dynamics. JOSA A. 25(1), 231-237 (2008).
4. Kirillin, M., Meglinski, I., Kuzmin, V., Sergeeva, E. & Myllylä, R. Simulation of optical coherence tomography images by Monte Carlo modeling based on polarization vector approach. Optics express 18(21), 21714-21724 (2010).
5. Doronin, A. & Meglinski, I. Online object oriented Monte Carlo computational tool for the needs of biomedical optics. Biomedical optics express 2(9), 2461-2469 (2011).
6. Munro, P.R., Curatolo, A. & Sampson, D.D. Full wave model of image formation in optical coherence tomography applicable to general samples. Optics express 23(3), 2541-2556 (2015).
7. Munro, P.R. Three-dimensional full wave model of image formation in optical coherence tomography. Optics express 24(23), 27016-27031 (2016).
8. Brenner, T., Munro, P.R., Krüger, B. & Kienle, A. Two-dimensional simulation of optical coherence tomography images. Scientific reports 9(1), 1-16 (2019).
9. Almasian, M., van Leeuwen, T. G. & Faber, D. J. OCT amplitude and speckle statistics of discrete random media. Scientific Reports 7, 14873 (2017).
10. Kalkman, J. Fourier-Domain Optical Coherence Tomography Signal Analysis and Numerical Modeling. International Journal of Optics 2017, 9586067 (2017).
11. Schmitt, J. M. & Knüttel, A. Model of optical coherence tomography of heterogeneous tissue. J. Opt. Soc. Am. A 14(6), 1231–1242 (1997).
12. Chin, L., et al. Analysis of image formation in optical coherence elastography using a multiphysics approach. Biomedical optics express 5(9), 2913-2930 (2014).
13. Abdurashitov, A. & Tuchin, V. A robust model of an OCT signal in a spectral domain. Laser Physics Letters 15(8), 086201 (2018).
14. Buligin, A.D., Kistenev, Y.V., Meglinski, I., Danilkin, E.A. & Vrazhnov, D.A. Imitation of ultra-sharp light focusing within turbid tissue-like scattering medium by using time-independent Helmholtz equation and method Monte Carlo. SPIE Proceedings 11582, 115821N (2020).
15. Cheng, X., et al. Development of a beam propagation method to simulate the point spread function degradation in scattering media. Optics letters 44(20), 4989-4992 (2019).
16. Zaitsev, V.Y., Matveev, L.A., Matveyev, A.L., Gelikonov, G.V. & Gelikonov, V.M. A model for simulating speckle-pattern evolution based on close to reality procedures used in spectral-domain OCT. Laser Physics Letters 11(10), 105601 (2014).
17. Matveyev, A.L., et al. Semi-analytical full-wave model for simulations of scans in optical coherence tomography with accounting for beam focusing and the motion of scatterers. Laser Physics Letters 16(8), 085601 (2019).

18. Matveyev, A.L., et al. Computationally efficient model of OCT scan formation by focused beams and its usage to demonstrate a novel principle of OCT-angiography. Laser Physics Letters 17(11), 115604 (2020).

19. Mariampillai, A., et al. Speckle variance detection of microvasculature using swept-source optical coherence tomography. Optics Letters 33(13), 1530–1532 (2008).

20. Zaitsev, V. Y., et al. Hybrid method of strain estimation in optical coherence elastography using combined sub-wavelength phase measurements and supra-pixel displacement tracking. Journal of Biophotonics 9(5), 499–509 (2016).

21. Zaitsev, V. Y., et al. Deformation induced speckle-pattern evolution and feasibility of correlational speckle tracking in optical coherence elastography. Journal of biomedical optics 20(7), 075006 (2015).

22. Zaitsev, V. Y., et al. Optimized phase gradient measurements and phase-amplitude interplay in optical coherence elastography. Journal of Biomedical Optics 21(11), 116005 (2016).

23. Zaitsev, V. Y., et al. Strain and elasticity imaging in compression optical coherence elastography: the two‐decade perspective and recent advances. Journal of Biophotonics 14(2), e202000257 (2020).

24. Ginner, L., et al. Noniterative digital aberration correction for cellular resolution retinal optical coherencetomography in vivo. Optica 4(8), 924-931 (2017).

25. Lakshminarayanan, V. & Fleck, A. Zernike polynomials: a guide. Journal of Modern Optics 58(7), 545-561 (2011).

26. Camino, A., et al. Depth-resolved optimization of a real-time sensorless adaptive optics optical coherence tomography. Optics letters 45(9), 2612-2615 (2020).

27. Borycki, D., Auksorius, E., Węgrzyn, P. & Wojtkowski, M. Computational aberration correction in spatiotemporal optical coherence (STOC) imaging. Optics letters 45(6), 1293-1296 (2020).

28. Matkivsky, V., et al. Determination and correction of aberrations in full field optical coherence tomography using phase gradient autofocus by maximizing the likelihood function. Journal of Biophotonics 13(10), e202000112 (2020).

29. Curatolo, A., et al. Ultrahigh-resolution optical coherence elastography. Optics Letters 41(1), 21-24 (2016).

30. Lee, K.-S. & Rolland, J. P. Bessel beam spectral-domain high-resolution optical coherence tomography with micro-optic axicon providing extended focusing range. Optics Letters 33(15), 1696-1698 (2008).

31. Moiseev A. A., et al. Digital refocusing in optical coherence tomography using finite impulse response filters. Laser Phys. Lett. 15, 095601 (2018).

32. Allen, W. M., et al. Wide-field optical coherence micro-elastography for intraoperative assessment of human breast cancer margins. Biomedical Optics Express 7(10), 4139–4152 (2016).

33. Kennedy, K. M., et al. Diagnostic Accuracy of Quantitative Micro-Elastography for Margin Assessment in Breast-Conserving Surgery. Cancer Research 80(8), 1773–1783 (2020).

34. Gubarkova, E. V., et al. OCT-elastography-based optical biopsy for breast cancer delineation and express assessment of morphological/molecular subtypes. Biomedical Optics Express 10(5), 2244 (2019).

35. Sirotkina, M. A., et al. In vivo assessment of functional and morphological alterations in tumors under treatment using OCT-angiography combined with OCT-elastography. Biomedical Optics Express 11(3), 1365 (2020).

36. Plekhanov, A. A., et al. Histological validation of in vivo assessment of cancer tissue inhomogeneity and automated morphological segmentation enabled by Optical Coherence Elastography. Scientific Reports 10(1), 11781 (2020).

37. Baum, O. I., et al. Interplay of temperature, thermal-stresses and strains in laser-assisted modification of collagenous tissues: Speckle-contrast and OCT-based studies. Journal of Biophotonics 13(1), e201900199 (2019).

38. Alexandrovskaya, Y. M., et al. Observation of internal stress relaxation in laser-reshaped cartilaginous implants using OCT-based strain mapping. Laser Physics Letters 17(8), 085603 (2020).

39. Lawman, S., et al. Deformation velocity imaging using optical coherence tomography and its applications to the cornea. Biomedical Optics Express 8(12), 5579-5593 (2017).

40. Kennedy, B. F., et al. Strain estimation in phase-sensitive optical coherence elastography. Biomedical Optics Express 3(8), 1865-1879 (2012).

41. Matveyev, A. L., et al. Vector method for strain estimation in phase-sensitive optical coherence elastography. Laser Physics Letters 15(6), 065603 (2018).

42. Zaitsev, V. Y., et al. Revealing structural modifications in thermomechanical reshaping of collagenous tissues using optical coherence elastography. Journal of Biophotonics 12(3), e201800250 (2019).

43. Kling, S. Optical coherence elastography by ambient pressure modulation for high-resolution strain mapping applied to patterned cross-linking. Journal of the Royal Society Interface 17(162), 20190786 (2020).

44. Singh, M., Nair, A., Aglyamov, S. R. & Larin, K. V. Compressional Optical Coherence Elastography of the Cornea. Photonics 8(4), 111 (2021).

45. Moiseev, A., et al. Optical coherence tomography ‐ based angiography device with real ‐ time angiography B ‐ scans visualization and hand ‐ held probe for everyday clinical use. Journal of biophotonics 11(10), e201700292 (2018).

46. Zykov, A. A., Matveyev, A. L., Matveev, L. A., Sovetsky, A. A. & Zaitsev, V. Y. Flexible computationally efficient platform for simulating scan formation in optical coherence tomography with accounting for arbitrary motions of scatterers. J Biomed. Photon.&Engineering 7(1), 010304 (2021)